





Activated chemical bonds in nanoporous and amorphous iridium oxides favor low overpotential for oxygen evolution reaction

Sangseob Lee ^{1,2}, Yun-Jae Lee ^{1,2}, Giyeok Lee ¹ & Aloysius Soon ¹✉

To date, the search for active, selective, and stable electrocatalysts for the oxygen evolution reaction (OER) has not ceased and a detailed atomic-level design of the OER catalyst remains an outstanding (if not, compelling) problem. Considerable studies on different surfaces and polymorphs of iridium oxides (with varying stoichiometries and dopants) have emerged over the years, showing much higher OER activity than the conventionally reported rutile-type IrO₂. Here, we have considered different metastable nanoporous and amorphous iridium oxides of different chemical stoichiometries. Using first-principles electronic structure calculations, we investigate the (electro)chemical stability, intercalation properties, and electronic structure of these iridium oxides. Using an empirical regression model between the Ir-O bond characteristics and the measured OER overpotentials, we demonstrate how activated Ir-O bonds (and the presence of more electrophilic oxygens) in these less understood polymorphs of iridium oxides can explain their superior OER performance observed in experiments.

¹Department of Materials Science & Engineering and Center for Artificial Synesthesia Materials Discovery, Yonsei University, Seoul 03722, Republic of Korea.

²These authors contributed equally: Sangseob Lee, Yun-Jae Lee. ✉email: aloyus.soon@yonsei.ac.kr

To achieve sustainable energy production, solar-driven (electro)conversion of CO₂ and H₂O to value-added solar fuels and O₂ is a promising means to correct the global carbon balance and provide a sustainable alternative to conventional fossil fuels^{1–3}. Here, the anodic reaction—commonly known as the oxygen evolution reaction (OER), is an important half-cell reaction where H₂O is catalytically split to evolve O₂. However, due to the intrinsic sluggish kinetics of the OER, this leads to an overall poor catalytic performance in general.

Thus, to improve the long-term efficacy of this anodic reaction, the search for active, selective, and stable OER electrocatalysts has been on the rise, and amongst them, oxides (and oxyhydroxides) of iridium and ruthenium are known for their outstanding stability and reactivity in acidic environments^{2,4}. A promising way to tune and engineer the structure–property relations of these oxide catalysts is to control their stoichiometry and polymorphic phase at the atomic-level^{5–9}.

Willinger et al. experimentally found that channel-like microstructures (resembling the hollandite- or romanechite-type motifs) contributed to a better OER efficiency and catalytic stability of the amorphous iridium oxide catalyst¹⁰. It was also reported that the intercalation of alkaline earth metal cations in the nanopores of these channel-type microstructures adds stability to the overall catalyst structure^{11–13}. Though these accounts demonstrate improved OER performance over conventional crystalline rutile-structured IrO₂, a fundamental atomic-scale understanding of these nanopore-containing amorphous iridium oxides is very much lacking. Thus, it greatly hinders the establishment of a design rule for further performance improvement.

In an effort to fill this lack, a very recent high-throughput computational study¹⁴ (assisted by an generalizable active-learning accelerated algorithm) has attempted to investigate the role of polymorphism in both IrO₂ and IrO₃ (and their surfaces) for OER activity. Using a machine-learning-based surrogate model, they were able to rationalize that under OER technical catalysis conditions, the α -phase of IrO₃ was, in fact, predicted to have higher thermodynamic stability and high OER activity, as compared to that of rutile-type IrO₂. However, nanoporous (i.e. crystal structures containing nanopores and nanochannels) and amorphous iridium oxides—which have been proposed in various experiments^{11–13}—have not been included nor examined in this study.

Moreover, from the OER reaction mechanistic point-of-view, there is still an ongoing debate as to whether the direct formation of O₂ molecule proceeds via the adsorbate evolving mechanism (AEM, where concerted electron–proton transfer steps are involved)^{15,16}, or by means of the lattice oxygen mechanism (LOM, where lattice oxygen participates via a Mars van Krevelen-type process)¹⁷. O isotope-labeling experiments have revealed and suggested that the LOM is more likely on the surface of IrO₂ where the Mars van Krevelen-type process has also been proposed for non-oxide compounds (e.g. in sulfides and chlorides)¹⁷. Specifically, for the LOM, it has been proposed in many reports that the presence of electrophilic oxygen on the surface of iridium oxide will play an important role in the adsorption of the nucleophilic H₂O molecule via the so-called flexible charge state of Ir cations in the different phases of iridium oxide^{10,18–21}.

In addition, the chemical characteristics of the Ir–O bond has been suggested as a key descriptor for both O₂ desorption and the adsorption of H₂O on iridium oxides¹⁵. In the same vein, the use of the metal–sulfur bond strength as a descriptor for Mars van Krevelen-type dehydrosulfurization has also been deliberated in a previous report¹⁷. These suggested atomistic features (e.g. the correlation between the flexibility of the charge state of Ir cations and the presence of electrophilic oxygen, and Ir–O bonding characteristic) are still poorly understood, especially for experimentally observed nanoporous and amorphous iridium oxides.

In this work, to bolster the work of Flores et al.¹⁴, we expand and include experimentally motivated IrO₂ polymorphs (such as nanoporous hollandite-, romanechite-, and todorokite-type IrO₂ with K-intercalation) as well as amorphous structures of iridium oxides of varying chemical stoichiometry. Here, using first-principles density-functional theory (DFT) calculations, we show that the nonequivalent connectivity in the amorphous iridium oxide structures greatly improves the flexibility of the Ir charge states, and hence promoting the presence of electrophilic oxygens in them, when compared to their crystalline counterparts. We also demonstrate that a Pauling-like relation between the Ir–O bond length versus bond strength for the Ir–O bonds exist in amorphous iridium oxides, corroborating with the proposal of flexible charges states and activated bonds for more efficient OER catalysis. Via an empirical regression model between the Ir–O bond characteristics and the measured OER overpotentials, we propose that these less understood metastable nanoporous and amorphous iridium oxides may indeed afford a lower OER overpotential, reconciling their superior OER catalytic performance in recent experiments.

Results

Crystalline and nanoporous phases of iridium oxides. Following a recent survey of iridium oxide polymorphs by machine learning approaches¹⁴, we have adopted the low-energy polymorphs of IrO₂ and IrO₃—namely, the rutile phase of IrO₂ (R-IrO₂; Fig. 1a), and the *R* $\bar{3}c$ (R-IrO₃; Fig. 1j) and *P*6₃22 (P-IrO₃; Fig. 1k) phases of IrO₃. In addition, we have also included the experimentally proposed MnO₂-like nanoporous structures of IrO₂^{10,12,13} (which were not included in the previous computational studies)—in particular, the hollandite (Ho-IrO₂), romanechite (Ro-IrO₂), and todorokite (To-IrO₂) phases (as presented in Fig. 1b, d, f, respectively). These nanoporous or nanochanneled oxide structures are typically intercalated with alkali metal ions to improve structural stability and have also been proposed to improve OER catalytic activities^{10,12}.

To take the ion intercalation into account, in Fig. 1c, e, g, we show the K ion intercalated IrO₂ hollandite structure (1K + Ho-IrO₂), the K ion intercalated IrO₂ romanechite structure (2K + Ro-IrO₂), and the K ion intercalated IrO₂ todorokite structure (4K + To-IrO₂), respectively. To further extend our theoretical investigation on non-stoichiometric iridium oxides, fictitious crystal structures of IrO_{1.5} (or Ir₂O₃) have been included in this work—namely the corundum phase (C-IrO_{1.5}; Fig. 1h) and the bixbyite phase (B-IrO_{1.5}; Fig. 1i).

Using the optB86b *xc* functional, we have computed the optimized lattice parameters (with the corresponding space groups) for all crystalline phases of IrO₂, IrO_{1.5}, and IrO₃ polymorphs and listed their values in Table 1. In our DFT calculations, the calculated lattice parameters are well within 1–2% agreement with available experimental values (e.g. the experimentally reported *a*, *b*, and *c* lattice constants for rutile R-IrO₂ are 4.51, 4.51, and 3.16 Å, respectively)²². It is worth noting that there has been a previous attempt to experimentally expound on the crystallography of the hollandite-type iridates²³. For the hollandite-type iridates, our DFT calculations consistently favor the lower symmetry monoclinic *C*2/*m* phase (as opposed to the tetragonal phase), regardless of ion intercalation. We also find that the volumetric changes to the intercalated nanoporous IrO₂ defer according to channel size. For instance, the volume of 2K + Ro-IrO₂ shrinks by about 3% while that of 4K + To-IrO₂ expands by about 5%.

Amorphous phases of iridium oxides. Besides the commonly reported crystalline phases of active IrO_x for OER, recent experimental reports of an amorphous IrO_x phase could well be responsible for the high OER activity observed^{12,20,24}. To generate

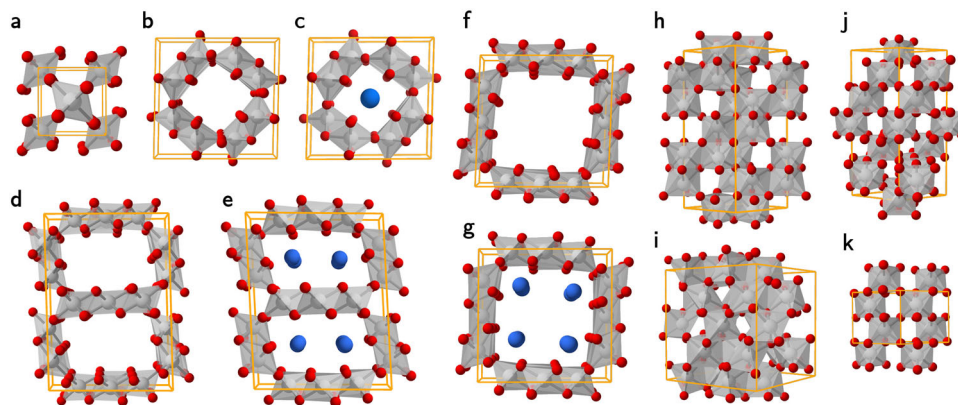


Fig. 1 Atomic and crystal structures of the crystalline iridium oxides. **a** Rutile-type R-IrO₂. **b** Hollandite-type Ho-IrO₂. **c** K-intercalated hollandite-type 1K + Ho-IrO₂. **d** Romanechite-type Ro-IrO₂. **e** K-intercalated romanechite-type 2K + Ro-IrO₂. **f** Todorokite-type To-IrO₂. **g** K-intercalated todorokite-type 4K + To-IrO₂. **h** Corundum-based C-IrO_{1.5}. **i** bixbyite-based B-IrO_{1.5}. **j** $R\bar{3}c$ R-IrO₃. **k** $P6_322$ P-IrO₃. The iridium, oxygen, and potassium atoms are depicted as gray, red, and blue spheres, respectively, while the octahedra of IrO₆ is shaded in gray. The bulk unit cell is represented by the lines in orange.

Table 1 Calculated lattice parameters, space group, and thermodynamic properties.

Ir-O system	<i>a</i> (Å)	<i>b</i> (Å)	<i>c</i> (Å)	β (°)	Space group	ΔH^f	ΔG_{300K}^f	ΔG_{600K}^f	ΔH_{int}^{int}
R-IrO ₂	4.51	4.51	3.19	90.0	$P4_2/mnm$	−0.97	−0.94	−1.03	
Ho-IrO ₂	10.24	3.19	9.95	91.0	$C2/m$	−0.80	−0.78	−0.88	
1K + Ho-IrO ₂	10.10	3.19	9.77	91.7	$C2/m$	−1.01	−0.99	−1.09	−3.52
Ro-IrO ₂	14.11	3.18	9.91	91.4	$C2/m$	−0.77	−0.75	−0.85	
2K + Ro-IrO ₂	13.11	3.20	10.24	93.3	$C2/m$	−1.03	−1.02	−1.13	−3.01
To-IrO ₂	9.88	3.17	9.79	92.1	$P2/m$	−0.74	−0.78	−0.83	
4K + To-IrO ₂	9.99	3.23	9.97	90.5	$P2/m$	−1.02	−1.01	−1.11	−2.28
<i>a</i> -IrO ₂	10.71	9.83	10.44		$P1$	−0.58	−0.56	−0.65	
C-IrO _{1.5}	5.27	13.90	5.27	120.0	$R\bar{3}c$	−0.48	−0.46	−0.56	
B-IrO _{1.5}	9.73	9.73	9.73	90.0	$Ia\bar{3}$	−0.37	−0.35	−0.45	
<i>a</i> -IrO _{1.5}	10.07	9.03	10.37		$P1$	−0.43	−0.41	−0.51	
R-IrO ₃	4.82	12.77	4.82	120.0	$R\bar{3}c$	−0.72	−0.69	−0.77	
P-IrO ₃	4.75	4.35	4.75	120.0	$P6_322$	−0.72	−0.69	−0.77	
<i>a</i> -IrO ₃	10.94	8.64	11.38		$P1$	−0.48	−0.45	−0.54	

Lattice parameters (*a*, *b*, and *c* are given in Å, and β in °), crystal space group, the formation energy (ΔH^f , given in eV/atom), the Gibbs energy of formation (ΔG^f , given in eV/atom for temperatures 300 and 600 K), and the intercalation energy (ΔH_{int}^{int} , given in eV/K atom) for the various iridium oxide systems.

approximate atomistic models of amorphous IrO_x, we perform *aiMD* calculations (following the melt-and-quench method²⁵) for various chemical stoichiometries (henceforth labeled as *a*-IrO₂, *a*-IrO_{1.5}, and *a*-IrO₃, accordingly) while ensuring numerical convergence with supercell size.

We calculate and plot the calculated partial radial distribution function, $g(r)$ of Ir–O (in black), O–O (in red), and Ir–Ir (in blue) bond pairs (cf. Supplementary Eq. (1) for *a*-IrO₂, *a*-IrO_{1.5}, and *a*-IrO₃ in Fig. 2. For all models presented here for amorphous iridium oxide, we do not observe any long-range ordering beyond 4 Å. For *a*-IrO₂, the representative $g(r)$ peaks (indicated by the vertical dashed lines; 2.00, 2.78, and 3.56 Å for the Ir–O, O–O, and Ir–Ir bond pairs) are shown in Fig. 2a, agreeing very well with the reported experimental values of 2.00 Å for the Ir–O bond distance^{10,12}. When considering the much larger supercell of 216 atoms (in Fig. 2b), we find that the representative $g(r)$ peaks are somewhat unchanged, and thus lending support that our smaller 96-atom supercell may be appropriate for modeling *a*-IrO₂. Likewise, for both *a*-IrO_{1.5} (in Fig. 2c, d) and *a*-IrO₃ (in Fig. 2e, f), similar agreement is met and we can draw the conclusion that amorphous iridium oxide yields an averaged Ir–O, O–O, and Ir–Ir bond distances of 2.0, 2.7, and 3.6 Å, respectively—irregardless of its chemical stoichiometry^{26,27}. Incidentally, we note that the very small $g(r)$ peak for *a*-IrO₃ near 1.5 Å is attributed to small oxygen clusters in the model.

In addition, the calculated mass densities for *a*-IrO₂, *a*-IrO_{1.5}, and *a*-IrO₃ are found to be 10.7, 12.2, and 8.9 g/cm³, respectively. When compared to the experimentally reported mass density of crystalline IrO₂ (i.e. 11.7 g/cm³),²⁸ our calculated value for *a*-IrO₂ appears somewhat smaller and this is inline with that found for other materials²⁹. This difference may be attributed to the lower average coordination number of cations in the amorphous phase when compared to the crystalline phase³⁰. Moreover, a weak correlation between our MD-determined mass densities and the oxygen content is also suggested from our calculations³¹.

Thermodynamic and electrochemical stability. To address the thermodynamic stability for the various iridium oxide structures we considered in this work, we calculate the formation enthalpy, ΔH^f , via Supplementary Eq. (2) and are tabulated in Table 1. From our calculations, agreeing with previous studies^{10,15}, rutile IrO₂ is found to be the thermodynamic ground state structure for iridium dioxide, while both R-IrO₃ ($R\bar{3}c$) and P-IrO₃ ($P6_322$) are the representative ground state structures for iridium trioxide (differing only by 1 meV/f.u.). For the hypothetical IrO_{1.5}, the corundum phase, C-IrO_{1.5} is taken as the lowest energy structure.

The nanoporous Ho-, Ro-, and To-IrO₂ are all found to be metastable with respect to rutile IrO₂ and additional stability is gained upon K intercalation. To analyze the intercalation

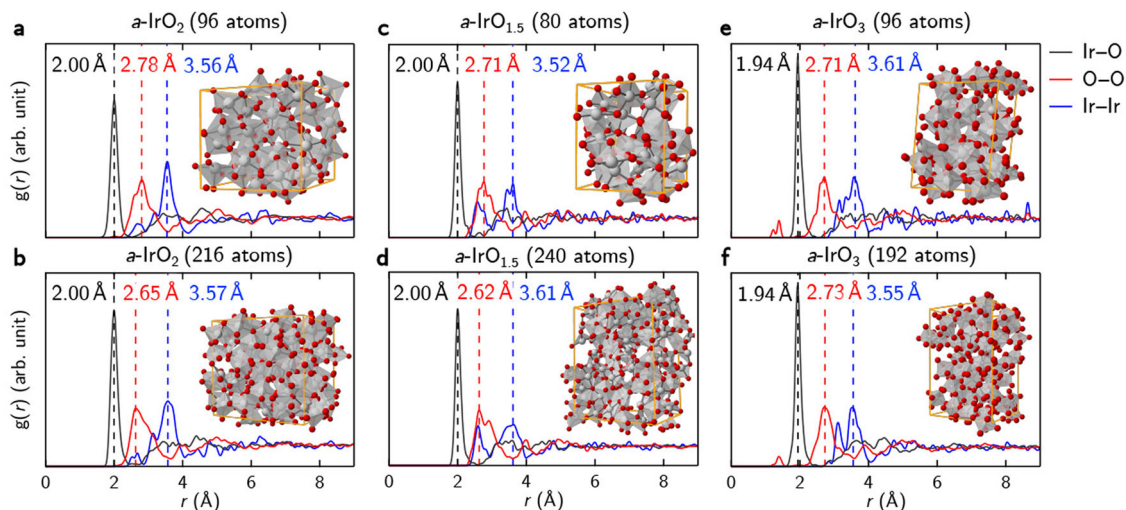


Fig. 2 Partial radial distribution function (RDF, $g(r)$) for the amorphous phases. **a, b** IrO_2 , **c, d** $\text{IrO}_{1.5}$, and **e, f** IrO_3 . The total number of atoms per simulation cell is shown for each case. The highest peak for the Ir-O, O-O, and Ir-Ir bond pair in the $g(r)$ is denoted by a vertical black, red, and blue dotted line, respectively. The optimized atomic structure for each amorphous iridium oxide phase is also shown, where the gray and red spheres represent the iridium and oxygen atoms, respectively. The simulation cell is represented by the solid lines in orange.

energetics in these nanoporous iridium oxide structures, we have also calculated their intercalation energy, ΔH^{int} (cf. Supplementary Eq. (4)) and are tabulated in Table 1. They are found to be largely exothermic and concur with earlier experimental and theoretical reports where cation intercalation in nanoporous oxides are known to add stability to the overall structure^{10,11,13,32,33}. Considering the amorphous analogs to these crystalline iridium oxides, $a\text{-IrO}_2$, $a\text{-IrO}_{1.5}$, and $a\text{-IrO}_3$ are also determined to be metastable with respect to their crystalline ground state counterparts. Thermodynamic metastability in other amorphous oxides (e.g. Sb_xO_y ²⁶) are well discussed in literature.

To account for thermal vibration contributions to the overall thermodynamic stability in these iridium oxides, using the Debye model, we estimate their vibrational energy, F^{vib} (cf. Supplementary Eq. (3)) and plot the variation of F^{vib} with temperature, T in the Supplementary Fig. 1. For comparison, we have also included the Gibbs energy of formation, ΔG^f for $T = 300$ and 600 K in Table 1. We conclude that thermal effects are minimal for the overall thermodynamic stability in these iridium oxides.

Now, to further discuss the stability of these oxides under technical catalysis or synthesis growth conditions, we examine their thermodynamic stability under an electrochemical environment^{5,34}. To do this, we construct the DFT-derived Pourbaix phase diagram by considering the reaction energy, $\Delta\mu$ and various relevant ionic species (cf. Supplementary Eq. (5) and Supplementary Table 1) and is presented in Fig. 3. Taking a recent experimental report¹⁰ as a reference, the ratio of K and Ir, and the concentration of the ion species are taken as 5:1 and 10^{-3} mol/L, respectively.

Within the considered range of pH and the electrode potentials in Fig. 3, marked as the shaded region (with gray lines), the thermodynamic ground state R- IrO_2 is predicted to be stable under low applied potentials and under both acidic and basic conditions. This is in accord with previous reports where the rutile IrO_2 phase exhibits good electrochemical stability¹⁴. However, under certain growth conditions that kinetically hinder the formation of the rutile phase, it is interesting to find that the metastable nanoporous Ho- IrO_2 phase can be synthesized within a relatively narrow window of stability (as in the turquoise shaded region in Fig. 3). More importantly, under more basic conditions as shown in the yellow shaded region of Fig. 3, $1\text{K} + \text{Ho-}\text{IrO}_2$ ($\text{K}_{0.25}\text{IrO}_2$) may form when assuming the kinetic hinderance of

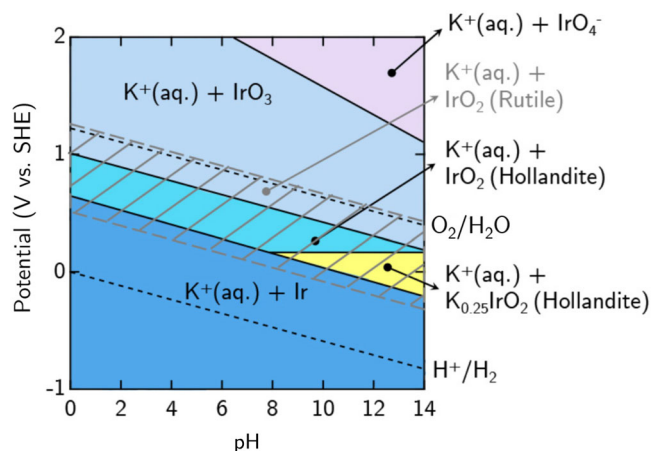


Fig. 3 DFT-derived Pourbaix phase diagram for the various iridium oxides and their K-intercalated phases. The shaded region (with gray lines) denotes the stability region for rutile IrO_2 . The standard potentials for water oxidation ($\text{O}_2^-/\text{H}_2\text{O}$) and reduction (H^+/H_2) are shown as black dotted lines. Following ref. ¹⁰, the ratio of K and Ir, and the concentration of the ion species are taken as 5:1 and 10^{-3} mol/L, respectively.

R- IrO_2 formation, and has been realized in recent electrochemical experiments^{10,12}. It has been argued that the residual presence of K^+ ions in the nanoporous framework of amorphous iridium oxide (containing local structures of $1\text{K} + \text{Ho-}\text{IrO}_2$) might improve the overall catalytic performance and stability¹⁰.

For much higher applied potentials, the calculated stability region of IrO_3 coincides well with previous studies¹⁴. Given that many non-equilibrium structures may be obtained by controlled synthesis conditions and a careful choice of reactants/precursors^{10,24}, we are hopeful that more metastable iridium oxides (e.g. the amorphous phases and other nanoporous structures; see Supplementary Fig. 2) can be investigated for their (electro)chemical stability.

Electronic structure. For the adsorption of the nucleophilic water molecule on the iridium oxide surface, the presence of an electrophilic oxygen atom may play a pivotal role as the susceptible

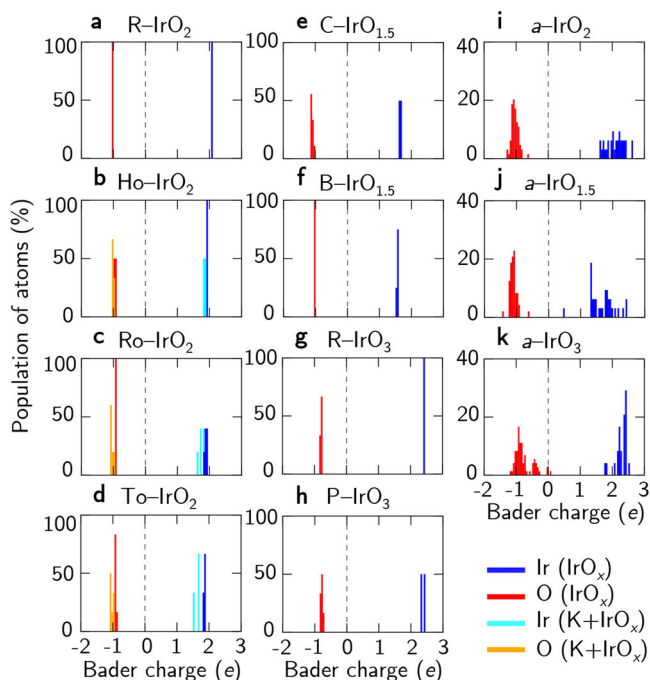


Fig. 4 Bader charge population of both Ir and O atoms. **a** R-IrO₂, **b** Ho-IrO₂, **c** Ro-IrO₂, **d** To-IrO₂, **e** C-IrO_{1.5}, **f** B-IrO_{1.5}, **g** R-IrO₃, **h** P-IrO₃, **i** *a*-IrO₂, **j** *a*-IrO_{1.5}, and **k** *a*-IrO₃. The Bader charge histogram for Ir and O atoms (without K) are denoted in blue and red bars, while that for Ir and O atoms in K-intercalated nanoporous iridium oxides are shown in cyan and yellow bars, respectively.

adsorption site to bind the water molecule on the iridium oxide surface^{4,15,18}. Here, we note that although the oxygen–oxygen bond formation does not necessarily involve the nucleophilic attack of a water molecule, following refs. ^{15,35,36}, we collectively combine both the nucleophilic water attack and the oxygen–oxygen bond formation within the same mechanistic step (cf. Supplementary Eq. (16)). In past literature, there have been several discussions on how the so-called flexibility of the charge state of iridium center atom in the IrO₆ octahedra (e.g. the varying ratio of Ir³⁺/Ir⁴⁺^{10,18}) is correlated to the enhanced activity of iridium oxides for OER. However, a clear theoretical consensus is yet to be reached. Moreover, an apparent relationship between the flexible charge state of Ir and its structural motifs (e.g. in nanoporous and amorphous iridium oxides) is still lacking.

To uncover the influence and relationship of the atomic charges of Ir and O atoms and the associated structural motifs, in Fig. 4, we first calculate and present the population histogram for the Bader charge of Ir and O atoms in the various iridium oxide systems. For R-IrO₂, the Bader charge of the Ir atom is calculated as +2.06e, while that of crystalline IrO_{1.5} and IrO₃ are determined to be between +1.52–+1.66 and +2.33–+2.42e, respectively. In the case of nanoporous IrO₂ polymorphs, the Bader charges of Ir are calculated to be within the range of +1.81–+1.93e, which is somewhat less than that in R-IrO₂ (+2.06e). Upon intercalation of K, the Bader charges of Ir (+1.52–+1.85e) are slightly reduced when compared to their pristine counterparts.

This reduction in the Bader charges of Ir can be correlated to the changes in the projected density-of-states (pDOS) for Ir in both the pristine and K-intercalated iridium oxides. In Supplementary Fig. 3, the Ir 5*d* states are calculated and plotted according to their Wyckoff positions. Noting the down-shift in the Ir 5*d* states to lower energy and the decreased Bader charges, it is indicative that electron transfer has occurred from the intercalated K atom to the nanoporous IrO₂ host structure¹².

Now, turning to the atomic charges of O atoms, we find a negative Bader charge value of $-1.04e$ for R-IrO₂, and the corresponding values for O atoms in crystalline IrO_{1.5}, and IrO₃ are between -1.14 to -1.02 and -0.85 to $-0.74e$, respectively. Here, we find that the oxygen atoms in the K-intercalated nanoporous iridium oxides become more nucleophilic (i.e. more negative in value) when compared to that of the pristine counterparts. For instance, the calculated Bader charges of O atoms in 1K + Ho-IrO₂ are between -1.05 to $-1.00e$, as compared to that in pristine Ho-IrO₂ (-0.99 to $-0.94e$). Referring to Fig. 4, similar trends are observed for 2K + Ro-IrO₂ and 4K + To-IrO₂. It now appears that K intercalation in these nanoporous iridium oxides adds extra thermodynamic stability but may not have a positive effect in generating more electrophilic oxygens needed for better OER performance.

Along the same vein of discussion, we notice a more flexible range of charge states for both the Ir and O atoms in the amorphous iridium oxides (namely, *a*-IrO₂, *a*-IrO_{1.5}, and *a*-IrO₃). From Fig. 4i, the Bader charges of Ir and O atoms of *a*-IrO₂ are calculated to be between +1.62–+2.61 and -1.29 to $-0.62e$, respectively (in contrast to +2.06 and $-1.04e$ for R-IrO₂). Similarly, the spread (hence, its flexibility) of the calculated Bader charges for *a*-IrO_{1.5} (Fig. 4j) and *a*-IrO₃ (Fig. 4k) are found to range between +0.47–+2.40 (for Ir) and -1.44 to $-0.64e$ (for O), and +1.75–+2.54 (for Ir) and -1.17 to $+0.12e$ (for O), respectively.

It is worth noting that the very small positive values in the Bader charges of O atoms for *a*-IrO₃ are attributed to oxygen clustering, as mentioned above. The variations in Bader charges of Ir atoms in amorphous iridium oxides are wider as compared to the crystalline and nanoporous analogs—indicating the possible presence of mixed valence states of Ir (i.e. Ir³⁺–Ir⁶⁺; see Supplementary Fig. 4) in these amorphous structures. It is clear that the diversity (or flexibility) found for the atomic charges can be attributed to the non-equivalent connectivity of the IrO_x polyhedra^{10,37}, given more severe local structural distortions/disorders can be found in these amorphous iridium oxides. Thus, results from our DFT calculations now gravitate towards the same deduction and observation reported in recent experiments where the flexibility of the charge state of Ir (hence, the possibility of electrophilic O species) is determined as a key descriptor for enhanced OER performance in amorphous iridium oxides^{18,19}.

Besides the adsorption of nucleophilic water molecules on the surface of the OER catalysts, the desorption/evolution of the oxygen molecule is also a dominant step in the LOM scheme of OER¹⁵. To tie the electronic structure argument back to its chemical bonding characteristics, we calculate and report the averaged projected crystal orbital Hamiltonian population (pCOHP; cf. Supplementary Eq. (6)) between the Ir and O atom pairs in these oxides in Fig. 5. We note that it is by convention to report the negative of these values³⁸. From the pCOHP, one can numerically discern the regions of bonding, anti-bonding, and non-bonding characteristics for a bond pair³⁹. Thus, one can infer the bonding nature and strength of the Ir–O bond which will be important in aiding the understanding of the atomic processes of OER on IrO_x catalysts. For the iridium oxide structures considered in this work, the Ir–O bond length ranges from 1.5 to 2.5 Å.

From Fig. 5, the anti-bonding states of the Ir–O bond (corresponding to the negative values of the $-pCOHP$ values) are found close to the Fermi-level for all iridium oxides. Upon K-intercalation for the nanoporous IrO₂ structures, a down-shift to lower energies in the pCOHP plot is observed, corroborating well with the pDOS in Supplementary Fig. 3. To further aid our ionic-covalent bonding character analysis^{37,40,41} in iridium oxides, we calculate the integrated pCOHP (IpCOHP) by integrating the pCOHP of specific bonding pairs of interest.

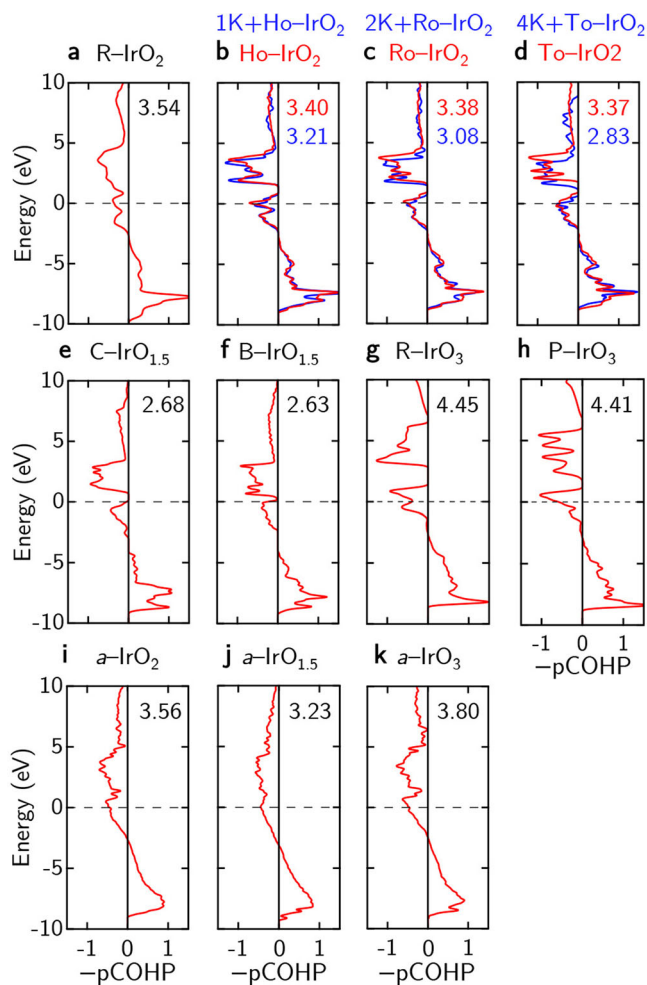


Fig. 5 Averaged projected crystal orbital Hamilton population ($-p\text{COHP}$) between the Ir and O atoms. **a** R-IrO₂, **b** Ho-IrO₂, **c** Ro-IrO₂, **d** To-IrO₂, **e** C-IrO_{1.5}, **f** B-IrO_{1.5}, **g** R-IrO₃, **h** P-IrO₃, **i** *a*-IrO₂, **j** *a*-IrO_{1.5}, and **k** *a*-IrO₃. For each $p\text{COHP}$ plot, the (negative) integrated $p\text{COHP}$ ($-\text{IpCOHP}$) values (up to the Fermi level) is also indicated in the top-right hand corner. For the case of nanoporous IrO₂, the $-p\text{COHP}$ curves and $-\text{IpCOHP}$ values are denoted red and blue for the pristine and K-intercalated structures, accordingly. The Fermi level is set to zero in all $p\text{COHP}$ plots.

We observe that the magnitude of the $-\text{IpCOHP}$ values for both the pristine and K-intercalated nanoporous IrO₂ is reduced compared to that of R-IrO₂, indicating a corresponding reduction in bond strength for the Ir–O bonds. Specifically, K-intercalation further reduces the $-\text{IpCOHP}$ values, alluding that the intercalation of K⁺ ions in hollandite-type IrO₂ is also experimentally shown to reduce the OER overpotential⁴². In the case of amorphous *a*-IrO₂, *a*-IrO_{1.5}, and *a*-IrO₃ (in Fig. 5i, j, k, respectively), a similar magnitude of the $-\text{IpCOHP}$ values is found as compared to that for R-IrO₂, while that of crystalline IrO_{1.5} (in Fig. 5g, h) are determined to be higher. This trend seems to corroborate with the expected valence of Ir in these oxides, with the amorphous iridium oxides displaying an intermediate value due to the flexible charge states of Ir, as outlined above.

Structure–property relationship and empirical regression model. Now, to make sense of the electronic structure, chemical bonding, and atomic structure of these iridium oxides of various stoichiometries and polymorphic forms, we will now plot the

specific $-\text{IpCOHP}$ values versus the Ir–O bond length for each given iridium oxide, considering the varying stoichiometries and polymorphic forms in Fig. 6a. The nonlinear relationship between the $-\text{IpCOHP}$ (i.e. the index for Ir–O bond strength) and Ir–O bond length nicely follows Pauling’s empirical relation on bond length versus bond strength^{37,41}, indicating that a longer bond would typically result in a weaker bond in a nonlinear fashion.

More importantly, from Fig. 6a, this nonlinear behavior is well captured for the amorphous iridium oxides where a wider assortment of strong/weak Ir–O bonds (hence, shorter/longer Ir–O bonds) is found. Unlike the amorphous oxides of iridium, their crystalline and nanoporous counterparts show a highly linear behavior for a narrower range of bond lengths and bond strengths. This provides a rather intuitive picture as to why in previously reported experiments^{10,18,19,21,43}, the amorphous forms of iridium oxide seem to outperform their crystalline analogs in OER. It is now evident that amorphous IrO_x of various stoichiometries can accommodate both strong and weak Ir–O bonds simultaneously to substantially provide sufficient thermodynamic stability and higher reactivity (e.g. in the case of OER), respectively. This then further lends support to the presence of flexible charge states of Ir (and thus, the ability to tailor a population of more electrophilic O species) in the amorphous iridium oxides, and explaining the enhancement in OER performance.

Extending this argument from the bulk phases of iridium oxides to their surfaces, we have chosen and constructed four different surface models—namely, R-IrO₂(110), Ho-IrO₂(100), *a*-IrO₂(001), and *a*-IrO_{1.5}(001)—and their calculated $-\text{IpCOHP}$ values as a function of Ir–O bond length are shown in Fig. 6a. Once again, the Pauling-like behavior for the surface bonds in these iridium oxides holds true and thus affords an appealing descriptor to discuss the impact of flexible bonds on the OER—even on the surfaces of these oxides. To address the ongoing debate as to whether the AEM or the LOM mechanism occurs on these iridium oxide surfaces, we calculate the Gibbs energy, ΔG for the AEM and LOM mechanistic steps³⁶ via the computational hydrogen electrode (CHE) approach⁴⁴ while considering the effect of surface coverages under reaction conditions^{45,46}. The Gibbs energy diagrams for O^{*}-covered Ho-IrO₂(100) and O^{*}-covered *a*-IrO_{1.5}(001) are presented in Fig. 6b, c, respectively. (The corresponding results for 2O_{CUS}^{*}-covered R-IrO₂(110) and O^{*}-covered *a*-IrO₂(001) can be found in Supplementary Fig. 7a, b. Further details are tabulated in Supplementary Tables 4 and 5).

Generally, for the crystalline phases of IrO₂ (including the nanoporous IrO₂ systems), the calculated value of η_{LOM} (~ 2 V) is almost two times larger than that of η_{AEM} (~ 1 V), as shown for O^{*}-covered Ho-IrO₂(100) in Fig. 6b and 2O_{CUS}^{*}-covered R-IrO₂(110) in Supplementary Fig. 7a. This is inline with previous theoretical calculations^{15,36}, and is in line with recent experiments⁴⁷ where the contribution of the LOM mechanism to the OER on polycrystalline IrO₂ is deemed negligible. In contrast, the calculated overpotential values for the amorphous (non) stoichiometric IrO₂ phases differ less (e.g. the calculated η_{AEM} and η_{LOM} for O^{*}-covered *a*-IrO_{1.5}(001) are 0.59 and 0.44 V, respectively; see Fig. 6c) and are lower in magnitude when compared to their crystalline counterparts. In the same vein of discussion, we deduce that the smaller (and more similar) values of η_{AEM} and η_{LOM} for OER on the amorphous IrO_x surfaces may stem from their ability to display a more flexible range of Ir–O bond lengths (and hence bond strengths) as captured by the Pauling’s empirical relation in Fig. 6a.

To provide a perspective of how activated Ir–O bonds (i.e. stretched Ir–O bonds) may be correlated to the overall OER performance, we put forth a simple linear regression model to

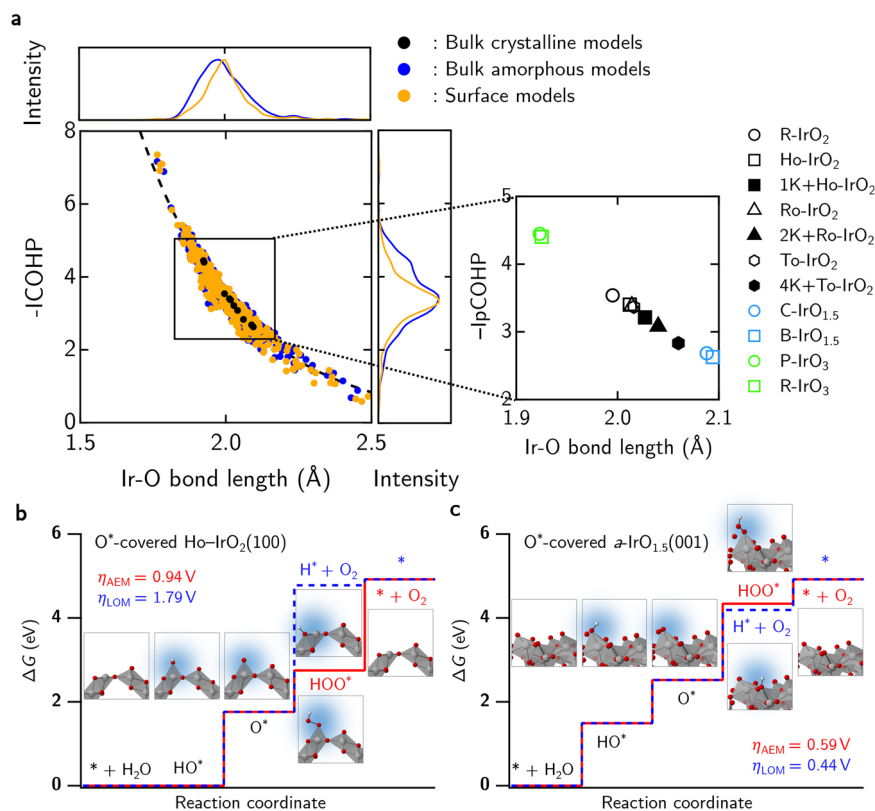


Fig. 6 Chemical and reaction steps analysis for oxygen evolution reaction on iridium oxides. **a** Scatterplot for $-\text{IpCOHP}$ versus Ir-O bond lengths for bulk crystalline and amorphous models and the surfaces of amorphous iridium oxides. The detailed plot for all crystalline/nanoporous iridium oxide phases are shown in the inset. The ΔG diagrams for OER via the adsorbate evolving mechanism (AEM; in red) and the lattice oxygen mechanism (LOM; in blue) for **b** O^{*}-covered Ho-IrO₂(100), and **c** O^{*}-covered α -IrO_{1.5}(001). The corresponding atomic structures for each reaction step are also provided alongside the ΔG diagrams. The iridium, oxygen, and hydrogen atoms are depicted as gray, red, and white spheres, respectively.

estimate the OER overpotential of these amorphous and nanoporous iridium oxides. From literature, we obtain the experimentally measured overpotential¹² for R-IrO₂ (0.40 V) and 1K + Ho-IrO₂ (0.34 V) and correlate that to our DFT-calculated $-\text{IpCOHP}$ for R-IrO₂ (3.54) and 1K + Ho-IrO₂ (3.21). From literature^{12,48–51}, we have further collected the measured OER overpotentials for various oxides—namely, RuO₂, SrIrO₃, Sr₂IrO₄, Sr₄IrO₆, CuFeO₃, SrFeO₃, and CaFeO₃—and performed $-\text{IpCOHP}$ calculations using their DFT-optimized lattice parameters (where the initial lattice constants are taken from the Materials Project database⁵²). Details of these values are tabulated in Table S3 of the Supplementary Information.

By using the experimentally measured overpotential values and our DFT-calculated $-\text{IpCOHP}$ values of bulk R-IrO₂, 1K + Ho-IrO₂, SrIrO₃, Sr₂IrO₄, and Sr₄IrO₆, a least-squared linear regression is plotted in Fig. 7a. In general, we find that RuO₂ and the iridates (SrIrO₃, Sr₂IrO₄, and Sr₄IrO₆) scatter close to the linear regression line while the ferrites (CuFeO₃, SrFeO₃, and CaFeO₃) deviate from this linear behavior, highlighting our simple regression line may capture the needed chemistry to estimate the OER potentials of iridium oxides studied in this work. In this line of argument, RuO₂ exhibits a larger overpotential due to stronger Ru–O bonds while the iridates may show comparable or even better OER performance as compared to the reference R-IrO₂.

Discussion

Using this empirical linear regression model (based on the Ir-based oxides), we can now empirically estimate the OER overpotential of the crystalline, nanoporous, and amorphous iridium

oxides from their corresponding calculated $-\text{IpCOHP}$ values. In particular, pristine nanoporous Ho-, Ro-, and To-IrO₂ are predicted to exhibit a slightly lowered overpotential of 0.37, 0.37, and 0.36 V, respectively, in comparison to experimentally measured overpotential 0.4 V for R-IrO₂¹². Upon K-intercalation, a further decrease in overpotential values to 0.32 and 0.29 V is seen for 2K + Ro-IrO₂ and 4K + To-IrO₂, respectively. For crystalline IrO_{1.5}, the estimated overpotential values are comparatively lower at 0.26 V while that for crystalline IrO₃ is the largest at 0.52 V.

For the bulk amorphous iridium oxides, given a Pauling-like non-linear variation of $-\text{IpCOHP}$ (in Fig. 6a), we take the statistical average (within the 90% confidence level) and plot the range of estimated overpotential values (as derived from the linear regression model) by considering the dispersion $-\text{IpCOHP}$ plots shown in side-panel graph in Fig. 6a. This leads to a very similar estimated OER overpotential value of 0.4 V as compared to the reference R-IrO₂. However, given the presence of flexible atomic charges and activated/stretched Ir–O bonds in these amorphous iridium oxides, a much lower limit of ~ 0.20 V may be attained (as estimated from the empirical linear regression model). This is qualitatively inline with our calculated overpotential trends when comparing the crystalline versus amorphous iridium oxide phases (Fig. 6b, c).

Combining this empirical regression model and the Pauling-like non-linear variation of $-\text{IpCOHP}$ versus bond length (for both bulk and surfaces of iridium oxides), a schematic perspective plot (Fig. 7b) may be drawn to illustrate this empirical relationship between the bond length, bond strength, and OER overpotential values where flexible charges states and activated bonds may explain highly efficient Ir-based OER catalysts.

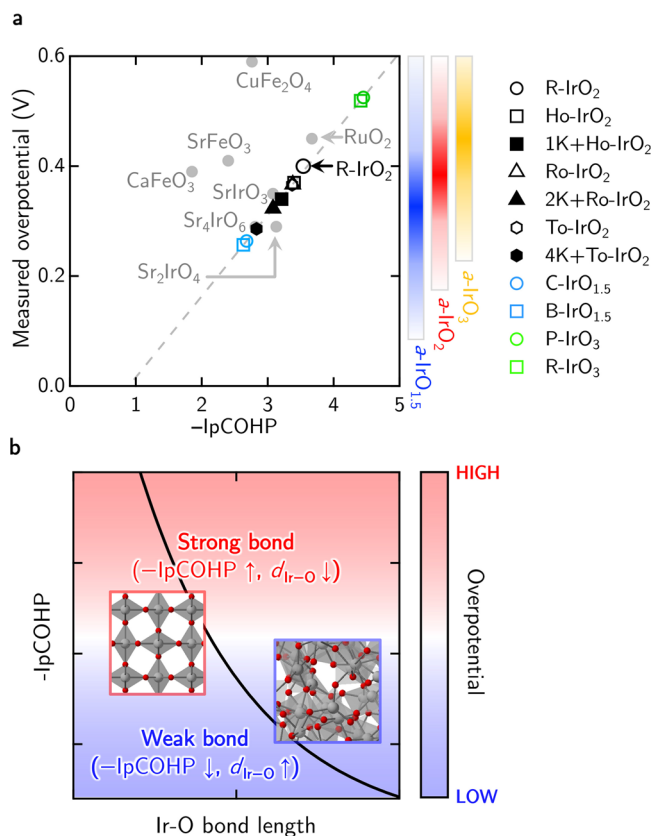


Fig. 7 Empirical regression model for structure-property relations in various OER oxide catalysts. **a** The experimental overpotentials of RuO_2 , SrIrO_3 , Sr_2IrO_4 , Sr_4IrO_6 , CuFeO_3 , SrFeO_3 , and CaFeO_3 are taken from refs. 48–51. The $-\text{lpCOHP}$ values are thus calculated from the Ir–O, Ru–O, or Fe–O bonding, accordingly. The gray dotted line is a least-square linear regression using values determined for R-IrO_2 , $1\text{K} + \text{Ho-IrO}_2$, SrIrO_3 , Sr_2IrO_4 , and Sr_4IrO_6 , with the corresponding R^2 value of 0.71. The range of overpotential values for the amorphous iridium oxides are provided from the linear regression model by considering the dispersion $-\text{lpCOHP}$ plots shown in side-panel graph. **b** Schematic view of the empirical relationship between Ir–O bond length, $-\text{lpCOHP}$, and overpotential. The iridium and oxygen atoms are depicted as gray and red spheres, respectively, while the IrO_6 octahedra is shaded in gray.

In conclusion, we have expanded and considered various nanoporous (with the inclusion of K-intercalation) and amorphous iridium oxides of different chemical stoichiometries. They are considered metastable with reference to the commonly reported ground state structures of IrO_2 and IrO_3 . This report marks the first time amorphous oxides of iridium are discussed. Under an electrochemical environment, we predict that the intercalation of K in nanoporous IrO_2 may be stable if the formation of rutile-type IrO_2 is kinetically hindered. When considering the atomic Bader charges of these IrO_x polymorphs, it becomes apparent that nonequivalent connectivity in the amorphous structures strongly enhance the flexibility of the charge states of Ir, and hence promoting the presence of electrophilic oxygens in them, as compared to their crystalline counterparts. Using the COHP-bonding analysis, we obtain a Pauling-like relation between the Ir–O bond length versus bond strength for the Ir–O bonds in amorphous iridium oxides while a fairly linear trend is found for the crystalline analogs. This also corroborates with the proposal of flexible charges states and activated bonds for more efficient OER catalysis. Lastly, using an empirical

regression model between the Ir–O bond characteristics and the measured OER overpotentials, we provide a perspective as to how these less understood metastable nanoporous and amorphous iridium oxides can offer a breakthrough in OER performance by a notable lowering of the anode overpotential. Here, we offer a fundamental atomistic picture to explain and reconcile the superior OER performance of sub-stoichiometric amorphous iridium oxides (where some channel-like microstructures have been observed) in recent OER experiments.

Methods

The DFT calculations are performed employing the projector augmented wave (PAW) method⁵³ as implemented in the Vienna Ab initio Simulation Package (VASP)^{54,55}. The 6s and 5d states of Ir, 2s and 2p states of O, and 3s, 3p, and 4s states of K are explicitly considered as the valence states within the PAW approach. The optB86b exchange–correlation (xc) functional is used, treating the DFT xc energy using a self-consistent van der Waals-corrected semi-local generalized gradient approximation⁵⁶. The optB86b xc functional has been shown to adequately describe various physicochemical properties of iridium oxides⁵⁷. All DFT calculations have been tested for convergence of kinetic energy cutoff and \mathbf{k} -points, where total energies and forces do not change more than 20 meV and 0.02 eV \AA^{-1} , respectively. A plane-wave kinetic energy cutoff of 500 eV and a Γ -centered \mathbf{k} -point grid spacing of 0.15 \AA^{-1} are used.

Ab initio molecular dynamics (aiMD) calculations are conducted at constant pressure (i.e. using the NPT ensemble) following the method of Parrinello and Rahman^{58,59}. The Langevin thermostat is used to control the temperature modulation with a friction coefficient of 10 ps^{−1}. To model the amorphous phases of iridium oxide with different stoichiometry, the 96-atom and 216-atom supercells of the cubic IrO_2 pyrite phase, the 80-atom cell $\text{IrO}_{1.5}$ bixbite phase, the 240-atom $\text{IrO}_{1.5}$ corundum phase, and the 96-atom and 192-atom supercells of the $R\bar{3}c$ phase of IrO_3 are adopted as initial atomic configurations for the respective stoichiometries. For these large supercell structures, the Brillouin zone is folded to the Γ -point and the kinetic cutoff energy is lowered to 300 eV. The initial structures are randomized at 3000 K for 10 ps (mimicking the melting process) and then quenched from 3000 to 100 K in 5 ps, with a cooling rate of 580K/ps. We further equilibrate the quenched structures at 300 K for another 10 ps in order to get more representative geometries at the temperature. For all aiMD calculations, a time step of 1 fs is used for the integration of the equations of motion.

The methods used to analyze the structural descriptors²⁵, the (electrochemical) thermodynamic stability, and chemical bonding and orbital population via the LOBSTER code^{38,60–63} are detailed in the Supplementary Information (SI).

Data availability

The data that support the findings of this study are available within the article and its supplementary information. Specifically, atomic structures generated in this work have been deposited in Zenodo under accession code <https://doi.org/10.5281/zenodo.5733499>.

Received: 12 July 2021; Accepted: 18 May 2022;

Published online: 08 June 2022

References

- Tahir, M. et al. Electrocatalytic oxygen evolution reaction for energy conversion and storage: a comprehensive review. *Nano Energy* **37**, 136–157 (2017).
- Shi, Z., Wang, X., Ge, J., Liu, C. & Xing, W. Fundamental understanding of the acidic oxygen evolution reaction: mechanism study and state-of-the-art catalysts. *Nanoscale* **12**, 13249–13275 (2020).
- Song, C. W., Lim, J., Bae, H. B. & Chung, S.-Y. Discovery of crystal structure–stability correlation in iridates for oxygen evolution electrocatalysis in acid. *Energy Environ. Sci.* **13**, 4178–4188 (2020).
- Schweinar, K., Gault, B., Mouton, I. & Kasian, O. Lattice oxygen exchange in rutile IrO_2 during the oxygen evolution reaction. *J. Phys. Chem. Lett.* **11**, 5008–5014 (2020).
- Lee, Y.-J., Lee, T. & Soon, A. Phase stability diagrams of group 6 magnéli oxides and their implications for photon-assisted applications. *Chem. Mater.* **31**, 4282–4290 (2019).
- Lee, Y.-J., Lee, T. & Soon, A. Over-stoichiometry in heavy metal oxides: the case of ionic-covalent tantalum trioxides. *Inorg. Chem.* **57**, 6057–6064 (2018).
- Jang, W., Yun, J., Lee, T., Lee, Y. & Soon, A. Disentangling the effects of inter- and intra-octahedral distortions on the electronic structure in binary metal trioxides. *J. Phys. Chem. C* **122**, 3558 (2018).

8. Lee, T., Lee, Y., Jang, W. & Soon, A. Understanding the advantage of hexagonal WO₃ as an efficient photoanode for solar water splitting: a first-principles perspective. *J. Mater. Chem. A* **4**, 11498–11506 (2016).
9. Yun, J., Jang, W., Lee, T., Lee, Y. & Soon, A. Aligning the band structures of polymorphic molybdenum oxides and organic emitters in light-emitting diodes. *Phys. Rev. Appl.* **7**, 024025 (2017).
10. Willinger, E., Massué, C., Schlögl, R. & Willinger, M. G. Identifying key structural features of IrO_x water splitting catalysts. *J. Am. Chem. Soc.* **139**, 12093–12101 (2017).
11. Young, M. J., Holder, A. M., George, S. M. & Musgrave, C. B. Charge storage in cation incorporated α -MnO₂. *Chem. Mater.* **27**, 1172–1180 (2015).
12. Sun, W., Song, Y., Gong, X.-Q., Cao, L.-M. & Yang, J. Hollandite structure K_{x=0.25}IrO₂ catalyst with highly efficient oxygen evolution reaction. *ACS Appl. Mater. Interfaces* **8**, 820–826 (2016).
13. Kitchaev, D. A., Dacek, S. T., Sun, W. & Ceder, G. Thermodynamics of phase selection in MnO₂ framework structures through alkali intercalation and hydration. *J. Am. Chem. Soc.* **139**, 2672–2681 (2017).
14. Flores, R. A. et al. Active learning accelerated discovery of stable iridium oxide polymorphs for the oxygen evolution reaction. *Chem. Mater.* **32**, 5854–5863 (2020).
15. Zagalskaya, A., Evazzade, I. & Alexandrov, V. Ab initio thermodynamics and kinetics of the lattice oxygen evolution reaction in iridium oxides. *ACS Energy Lett.* **6**, 1124–1133 (2021).
16. Fierro, S., Nagel, T., Baltruschat, H. & Comninellis, C. Investigation of the oxygen evolution reaction on Ti/IrO₂ electrodes using isotope labelling and on-line mass spectrometry. *Electrochem. Commun.* **9**, 1969–1974 (2007).
17. Doornkamp, C. & Ponc, V. The universal character of the Mars and Van Krevelen mechanism. *J. Mol. Catal. A Chem.* **162**, 19–32 (2000).
18. Pfeifer, V. et al. The electronic structure of iridium oxide electrodes active in water splitting. *Phys. Chem. Chem. Phys.* **18**, 2292–2296 (2016).
19. Pfeifer, V. et al. Reactive oxygen species in iridium-based OER catalysts. *Chem. Sci.* **7**, 6791–6795 (2016).
20. Ruiz Esquiús, J., Morgan, D. J., Spanos, I., Hewes, D. G., Freakley, S. J. & Hutchings, G. J. Effect of base on the facile hydrothermal preparation of highly active IrO_x oxygen evolution catalysts. *ACS Appl. Energy Mater.* **3**, 800–809 (2020).
21. Nong, H. N. et al. Key role of chemistry versus bias in electrocatalytic oxygen evolution. *Nature* **587**, 408 (2020).
22. Bolzan, A. A., Fong, C., Kennedy, B. J. & Howard, C. J. Structural studies of rutile-type metal dioxides. *Acta Crystallogr. Sect. B: Struct. Sci.* **53**, 373 (1997).
23. Talanov, A., Phelan, W. A., Kelly, Z. A., Siegler, M. A. & McQueen, T. M. Control of the iridium oxidation state in the hollandite iridate solid solution K_{1-x}Ir₄O₈. *Inorg. Chem.* **53**, 4500–4507 (2014).
24. Gao, J. et al. Breaking long-range order in iridium oxide by alkali ion for efficient water oxidation. *J. Am. Chem. Soc.* **141**, 3014–3023 (2019).
25. Lee, Y., Lee, T. & Soon, A. Polytropy in hexagonal tungsten trioxide: insights from ab initio molecular dynamics simulations. *J. Phys. Chem. C* **122**, 21644–21650 (2018).
26. Kim, C.-E., Skelton, J. M., Walsh, A. & Soon, A. Solid-state chemistry of glassy antimony oxides. *J. Mater. Chem. C* **3**, 11349–11356 (2015).
27. Riffet, V. & Vidal, J. Statistics-based analysis of the evolution of structural and electronic properties of realistic amorphous alumina during the densification process: insights from First-Principles approach. *J. Phys. Chem. C* **121**, 24745–24758 (2017).
28. Smith, R. D., Sporinova, B., Fagan, R. D., Trudel, S. & Berlinguette, C. P. Facile photochemical preparation of amorphous iridium oxide films for water oxidation catalysis. *Chem. Mater.* **26**, 1654 (2014).
29. Cui, X.-Y., Ringer, S. P., Wang, G. & Stachurski, Z. What Should the density of amorphous solids be? *J. Chem. Phys.* **151**, 194506 (2019).
30. Momida, H. et al. Theoretical study on dielectric response of amorphous alumina. *Phys. Rev. B* **73**, 054108 (2006).
31. Besozzi, E. et al. Thermomechanical properties of amorphous metallic tungsten–oxygen and tungsten-oxide coatings. *Mater. Des.* **165**, 107565 (2019).
32. Tompsett, D. A. & Islam, M. S. Electrochemistry of Hollandite α -MnO₂: Li-Ion and Na-Ion insertion and Li₂O incorporation. *Chem. Mater.* **25**, 2515–2526 (2013).
33. Yuan, Y. et al. Asynchronous crystal cell expansion during lithiation of K⁺-stabilized α -MnO₂. *Nano Lett.* **15**, 2998–3007 (2015).
34. Lee, G., Lee, Y.-J., Palotás, K., Lee, T. & Soon, A. Atomic structure and work function modulations in two-dimensional ultrathin CuI films on Cu(111) from First-Principles calculations. *J. Phys. Chem. C* **124**, 16362–16370 (2020).
35. Zhou, J. et al. Voltage- and time-dependent valence state transition in cobalt oxide catalysts during the oxygen evolution reaction. *Nat. Commun.* **11**, 1–10 (2020).
36. Zagalskaya, A. & Alexandrov, V. Role of defects in the interplay between adsorbate evolving and lattice oxygen mechanisms of the oxygen evolution reaction in RuO₂ and IrO₂. *ACS Catal.* **10**, 3650–3657 (2020).
37. Mocanu, F. C., Konstantinou, K., Mavračić, J. & Elliott, S. R. On the chemical bonding of amorphous Sb₂Te₃. *Phys. Status Solidi RRL* **15**, 2000485 (2021).
38. Dronskowski, R. & Bloechl, P. E. Crystal orbital Hamilton populations (COHP): energy-resolved visualization of chemical bonding in solids based on Density-functional calculations. *J. Phys. Chem.* **97**, 8617–8624 (1993).
39. Lee, J., Kim, H., Lee, T., Jang, W., Lee, K. H. & Soon, A. Revisiting polytypism in hexagonal ternary sulfide ZnIn₂S₄ for photocatalytic hydrogen production within the Z-scheme. *Chem. Mater.* **31**, 9148–9155 (2019).
40. Yoo, S.-H., Na, Y., Hwang, W., Jang, W. & Soon, A. First-Principles calculations of heteroanionic monochalcogenide alloy nanosheets with direction-dependent properties for anisotropic optoelectronics. *ACS Appl. Nano Mater.* **4**, 5912–5920 (2021).
41. Deringer, V. L., Stoffel, R. P., Wuttig, M. & Dronskowski, R. Vibrational properties and bonding nature of Sb₂Se₃ and their implications for chalcogenide materials. *Chem. Sci.* **6**, 5255–5262 (2015).
42. Sun, W., Song, Y., Gong, X.-Q., Cao, L.-M. & Yang, J. An Efficiently tuned D-orbital occupation of IrO₂ by doping with Cu for enhancing the oxygen evolution reaction activity. *Chem. Sci.* **6**, 4993–4999 (2015).
43. Saveleva, V. A. et al. Operando evidence for a universal oxygen evolution mechanism on thermal and electrochemical iridium oxides. *J. Phys. Chem. Lett.* **9**, 3154–3160 (2018).
44. Man, I. C. et al. Universality in oxygen evolution electrocatalysis on oxide surfaces. *ChemCatChem* **3**, 1159–1165 (2011).
45. Garca-Melchor, M., Vilella, L., López, N. & Vojvodic, A. Computationally probing the performance of hybrid, heterogeneous, and homogeneous iridium-based catalysts for water oxidation. *ChemCatChem* **8**, 1792–1798 (2016).
46. Rossmel, J., Qu, Z.-W., Zhu, H., Kroes, G.-J. & Nørskov, J. Electrolysis of water on oxide surfaces. *J. Electroanal. Chem.* **607**, 83–89 (2007).
47. Kasian, O. et al. Degradation of iridium oxides via oxygen evolution from the lattice: correlating atomic scale structure with reaction mechanisms. *Energy Environ. Sci.* **12**, 3548–3555 (2019).
48. Lee, Y., Suntovich, J., May, K. J., Perry, E. E. & Shao-Horn, Y. Synthesis and activities of rutile IrO₂ and RuO₂ nanoparticles for oxygen evolution in acid and alkaline solutions. *J. Phys. Chem. Lett.* **3**, 399–404 (2012).
49. Yagi, S. et al. Covalency-reinforced oxygen evolution reaction catalyst. *Nat. Commun.* **6**, 1–6 (2015).
50. Li, M. et al. Facile synthesis of electrospun MFe₂O₄ (M = Co, Ni, Cu, Mn) spinel nanofibers with excellent electrocatalytic properties for oxygen evolution and hydrogen peroxide reduction. *Nanoscale* **7**, 8920–8930 (2015).
51. Strickler, A. L., Higgins, D. & Jaramillo, T. F. Crystalline strontium iridate particle catalysts for enhanced oxygen evolution in acid. *ACS Appl. Energy Mater.* **2**, 5490–5498 (2019).
52. Jain, A. et al. The Materials Project: a materials genome approach to accelerating materials innovation. *APL Mater.* **1**, 011002 (2013).
53. Kresse, G. & Joubert, D. From ultrasoft pseudopotentials to the projector augmented-wave method. *Phys. Rev. B* **59**, 1758 (1999).
54. Kresse, G. & Hafner, J. Ab initio molecular dynamics for liquid metals. *Phys. Rev. B* **47**, 558 (1993).
55. Kresse, G. & Furthmüller, J. Efficient iterative schemes for ab initio total-energy calculations using a plane-wave basis set. *Phys. Rev. B* **54**, 11169 (1996).
56. Klimeš, J., Bowler, D. R. & Michaelides, A. Chemical accuracy for the Van Der Waals density functional. *J. Phys.: Condens. Matter* **22**, 022201 (2009).
57. Ping, Y., Galli, G. & Goddard, W. A. III Electronic structure of IrO₂: the role of the metal d orbitals. *J. Phys. Chem. C* **119**, 11570 (2015).
58. Parrinello, M. & Rahman, A. Crystal structure and pair potentials: a molecular-dynamics study. *Phys. Rev. Lett.* **45**, 1196 (1980).
59. Parrinello, M. & Rahman, A. Polymorphic transitions in single crystals: a new molecular dynamics method. *J. Appl. Phys.* **52**, 7182 (1981).
60. Deringer, V. L., Tchougréeff, A. L. & Dronskowski, R. Crystal orbital Hamilton population (COHP) analysis as projected from plane-wave basis sets. *J. Phys. Chem. A* **115**, 5461–5466 (2011).
61. Maintz, S., Deringer, V. L., Tchougréeff, A. L. & Dronskowski, R. Analytic projection from plane-wave and PAW wavefunctions and application to chemical-bonding analysis in solids. *J. Comput. Chem.* **34**, 2557–2567 (2013).
62. Maintz, S., Deringer, V. L., Tchougréeff, A. L. & Dronskowski, R. LOBSTER: a tool to extract chemical bonding from plane-wave based DFT. *J. Comput. Chem.* **37**, 1030–1035 (2016).
63. Nelson, R. et al. LOBSTER: local orbital projections, atomic charges, and chemical-bonding analysis from projector-augmented-wave-based Density-functional theory. *J. Comput. Chem.* **41**, 1931–1940 (2020).

Acknowledgements

S.L., Y.J.L., and G.L. gratefully acknowledge support from the Basic Science Research Program through the National Research Foundation of Korea (NRF 2020R1F1A1063070). Computational resources have been kindly provided by the Korean

Institute of Science and Technology Information (KISTI) Supercomputing Center (KSC-2021-CRE-0044) and the Australian National Computational Infrastructure (NCI).

Author contributions

S.L., Y.J.L., and G.L. constructed the atomistic models and performed the calculations. A.S. conceptualized and supervised this work. All authors were involved in the drafting of the manuscript.

Competing interests

The authors declare no competing interests.

Additional information

Supplementary information The online version contains supplementary material available at <https://doi.org/10.1038/s41467-022-30838-y>.

Correspondence and requests for materials should be addressed to Aloysius Soon.

Peer review information Nature Communications thanks the anonymous reviewers for their contribution to the peer review of this work.

Reprints and permission information is available at <http://www.nature.com/reprints>

Publisher's note Springer Nature remains neutral with regard to jurisdictional claims in published maps and institutional affiliations.



Open Access This article is licensed under a Creative Commons Attribution 4.0 International License, which permits use, sharing, adaptation, distribution and reproduction in any medium or format, as long as you give appropriate credit to the original author(s) and the source, provide a link to the Creative Commons license, and indicate if changes were made. The images or other third party material in this article are included in the article's Creative Commons license, unless indicated otherwise in a credit line to the material. If material is not included in the article's Creative Commons license and your intended use is not permitted by statutory regulation or exceeds the permitted use, you will need to obtain permission directly from the copyright holder. To view a copy of this license, visit <http://creativecommons.org/licenses/by/4.0/>.

© The Author(s) 2022